Table 1 Conversion efficiencies to NH₃ from NO₂⁻ and NO₃⁻ solutions in contact with catalysts

Mineral	Compound	T (°C)	Time (h)	Solution type	Product yield (%)
$Fe_{(1-x)}S$	NO_3^-	300	24	H_2O	53
$Fe_{(1-x)}S$	NO_2^-	300	24	H_2O	21
$Fe_{(1-x)}S$	NO_3^-	500	24	H_2O	73
$Fe_{(1-x)}S$	NO_2^-	500	24	H_2O	37
$Fe_{(1-x)}S$	NO_3^-	700	24	H_2O	89
$Fe_{(1-x)}S$	NO_2^-	700	24	H_2O	74
$Fe_{(1-x)}S$	NO_2^-	900	24	H_2O	0
$Fe_{(1-x)}S$	NO_3^-	500	0.033	H_2O	74
FeS_2	NO_3^-	500	24	H_2O	70
95%Fe,5%Ni	NO_3^-	500	24	H_2O	41
95%Fe,5%Ni	NO_2^-	500	24	H_2O	45
Fe_3O_4	NO_3^-	900	24	H_2O	0
Fe_3O_4	NO_3^-	500	24	H_2O	46
Fe_3O_4	NO_2^-	500	24	H_2O	9.4
Fe_3O_4	NO_3^-	500	0.033	H_2O	4.1
Fe_3O_4	NO_2^-	500	0.033	H_2O	1.0
Basalt	NO_3^-	500	24	H_2O	20
Basalt	NO_2^-	500	24	H_2O	14
$Fe_{(1-x)}S$	NO_3^-	500	24	Sea water	84
Fe_3O_4	NO_3^-	500	24	Sea water	1.2
Basalt	NO_3^-	500	24	Sea water	1.0

therefore have provided an early boost to oceanic NH₃ concentrations, and thus improved the prospects for synthesis and stability of N-containing organic compounds[21]. The results discussed here point to a probably oceanic or hydrothermal source for a large fraction of reduced nitrogen. Steady-state oceanic NH₃ concentrations would have depended on atmospheric loss rates[3,11]; locally, however, hydrothermal environments and adjacent waters would clearly have exhibited the highest NH₃ concentrations in the prebiotic world. After the genesis of life, hydrothermal environments would have continued to be oases, providing NH₃ to early life forms until the advent of enzymatic systems capable of reducing NO_3^- and N_2 (ref. 22).

Last, these results on potential sources of ocean NH₃ must be factored into estimates of the NH₃ content of the Archaean atmosphere. Even low concentrations of atmospheric NH₃ could be of great importance to photolytically driven organic synthesis[1]. Furthermore, Sagan and Chyba[3] have demonstrated that an atmospheric mixing ratio of 10^{-5} for ammonia would have been sufficient, through greenhouse warming, to resolve the early-faint-Sun paradox. Maintenance of this mixing ratio over the first 10^9 years of the Earth would have required a supply of 1.4×10^{18} g NH₃ (ref. 3). These results indicate that mineral-catalysed synthesis of NH₃ could have met at least one-third of this requirement, with the possibility that all of the necessary supply could have been produced in this manner if one assumes a highly reducing lithosphere during the Hadean. □

Methods

All experiments were run in sealed, N₂-purged, acid-washed, pure gold tubes. Iron sulphide and iron-metal catalysts were prepared from semiconductor-grade metals and pure elemental sulphur, with elemental compositions verified by ion-probe analysis. Magnetite catalyst was a very pure natural sample of fumarolic origin[23], whereas the basalt used was a natural alkali basalt (65992, ref. 28). Solution phases added to N₂ reduction capsules were either distilled deionized water or mixtures of formic acid and water. Solutions phases for NO_3^- and NO_2^- were 5 mM in either distilled deionized water or low-nutrient sea water. Tubes were loaded, purged with N₂ gas, welded shut and incubated in an internally heated pressure vessel under argon-medium[24,25]. Tubes were opened, extracted with distilled water and analysed for NO_3^-, NO_2^- and NH₃ by spectrophotometric methods[26,27].

1. Schlesinger, G. & Miller, S. L. Prebiotic synthesis in atmospheres containing CH₄, CO and CO₂. I. Amino acids. *J. Mol. Evol.* **19**, 376–383 (1983).
2. Stribling, R. & Miller, S. L. Energy yields for hydrogen cyanide and formaldehyde syntheses: the HCN and amino acid concentrations in the primitive ocean. *Origins Life Evol. Biosph.* **17**, 261–273 (1987).
3. Sagan, C. & Chyba, C. The early faint sun paradox: organic shielding of ultraviolet-labile greenhouse gases. *Science* **276**, 1217–1221 (1997).
4. Kasting, J. F., Eggler, D. H. & Raeburn, S. P. Mantle redox evolution and the oxidation state of the Archaean atmosphere. *J. Geol.* **101**, 245–257 (1993).
5. Berndt, M. E., Allen, D. E. & Seyfried, W. E. Jr Reduction of CO₂ during serpentization of olivine at 300 °C and 500 bar. *Geology* **24**, 351–354 (1996).
6. Tamaru, K. in *Catalytic Ammonium Synthesis* (ed. Jennings, J. R.) 1–18 (Plenum, New York, 1991).
7. Holland, H. D. *The Chemical Evolution of the Atmosphere and Oceans* (Princeton Univ. Press, 1984).
8. Frost, B. R. Stability of oxide minerals in metamorphic rocks. *Rev. Minerol.* **25**, 469–483 (1991).
9. Johnson, M. C., Anderson, A. T. Jr & Rutherford, M. J. Pre-eruptive volatile contents of magmas. *Rev. Minerol.* **30**, 281–330 (1994).
10. Javoy, M. & Pineau, F. The volatiles record of a 'popping' rock from the mid-Atlantic ridge at 14° N: chemical and isotopic composition of gas trapped in the vesicles. *Earth Planet. Sci. Lett.* **107**, 598–611 (1991).
11. Summers, D. P. & Chang, S. Prebiotic ammonia from reduction of nitrite by iron (II) on the early Earth. *Nature* **365**, 630–632 (1990).
12. Mancineli, R. L. & McKay, C. P. The evolution of nitrogen cycling. *Origins Life Evol. Biosph.* **18**, 311–326 (1990).
13. Buresh, R. J. & Moraghan, J. T. Chemical reduction of nitrate by ferrous iron. *J. Environ. Qual.* **5**, 320–325 (1976).
14. Knowles, R. Denitrification. *Microbiol. Rev.* **46**, 43–70 (1982).
15. Blöchl, E., Keller, M., Wachershauser, G. & Stetter, K. O. Reactions depending on iron sulfide and linking geochemistry with biochemistry. *Proc. Natl Acad. Sci. USA* **89**, 8117–8120 (1992).
16. Fournier, R. O. Conceptual models of brine evolution in magmatic hydrothermal systems. *US Geol. Surv. Prof. Pap.* **1350**, 1487–1506 (1987).
17. Stevenson, D. J. in *Earth's Earliest Biosphere: Its Origin and Evolution* (ed. Schopf, J. W.) 32–40 (Princeton Univ. Press, 1983).
18. Pizzarello, S., Feng, X., Epstein, S. & Cronin, J. R. Isotopic analyses of nitrogenous compounds from the Murchinson meteorite: ammonia, amines, amino acids, and polar hydrocarbons. *Geochim. Cosmochim. Acta* **58**, 5579–5587 (1994).
19. Zhang, Y. & Zindler, A. Distribution and evolution of carbon and nitrogen in Earth. *Earth Planet. Sci. Lett.* **117**, 331–345 (1993).
20. Henderson-Sellers, A. & Schwartz, A. W. Chemical evolution and ammonia in the early Earth's atmosphere. *Nature* **287**, 526–528 (1980).
21. Bada, J. L. & Miller, S. L. Ammonium ion concentration in the primitive ocean. *Science* **159**, 423–425 (1968).
22. Falkowski, P. G. & Raven, J. in *Aquatic Photosynthesis* Ch. 10 (Blackwell Science, Oxford, 1997).
23. Zeis, E. G. The fumarolic incrustations in the valley of ten thousand smokers. *Nat. Geol. Soc. Cont. Tech. Papers, Katmai Series* **1**, no. 3 (National Geographic Society, Washington, 1924).
24. Yoder, H. S. High–low quartz inversion up to 10,000 bars. *Trans. Am. Geophys. Union* **31**, 821–835 (1950).
25. Kullerud, G. & Yoder, H. S. Pyrite stability in the Fe–S system. *Econ. Geol.* **54**, 534–550 (1959).
26. Strickland, J. D. H. & Parsons, T. R. *A Practical Handbook of Seawater Analysis* (Fisheries Research Board of Canada, Ottawa, 1972).
27. Jones, M. N. Nitrate reduction by shaking with cadmium. *Water Res.* **18**, 643–646 (1984).
28. Yoder, H. S. & Tilley, C. E. Origin of basalt magmas: an experimental study of natural and synthetic rock systems. *J. Petrol.* **3**, 342–532 (1962).

Quantification of dust-forced heating of the lower troposphere

P. Alpert*, Y. J. Kaufman†, Y. Shay-El*, D. Tanre‡, A. da Silva§, S. Schubert§ & J. H. Joseph*

* *Department of Geophysics and Planetary Sciences, Tel-Aviv University, Israel 69978*
† *Climate and Radiation Branch, Code 913, NASA/GSFC, Greenbelt, Maryland 20771, USA*
‡ *Laboratoire d'Optique Atmosphérique, Bât. P5, UST de Lille, 59655-Villeneuve d'Ascq Cedex, France*
§ *Data Assimilation Office, Code 910.3, NASA/GSFC, Greenbelt, Maryland 20771, USA*

Aerosols may affect climate through the absorption and scattering of solar radiation and, in the case of large dust particles, by interacting with thermal radiation[1-3]. But whether atmospheric temperature responds significantly to such forcing has not been determined; feedback mechanisms could increase or decrease the effects of the aerosol forcing. Here we present an indirect measure of the tropospheric temperature response by explaining the 'errors' in the NASA/Goddard model/data-assimilation system. These errors, which provide information about physical processes

missing from the predictive model, have monthly mean patterns that bear a striking similarity to observed patterns of dust over the eastern tropical North Atlantic Ocean. This similarity, together with the high correlations between latitudinal location of inferred maximum atmospheric heating rates and that of the number of dusty days, suggests that dust aerosols are an important source of inaccuracies in numerical weather-prediction models in this region. For the average dust event, dust is estimated to heat the lower atmosphere (1.5–3.5 km altitude) by ~0.2 K per day. At about 30 dusty days per year, the presence of the dust leads to a regional heating rate of ~6 K per year.

It is widely held that cloud and water processes are predominant in prescribing climate model errors[4]. For instance, the ability of the general circulation models (GCMs) to describe faithfully the transport of water vapour into the upper troposphere by well developed clouds is a central point in the debate on the ability of GCMs to predict the atmospheric warming due to the doubling of atmospheric CO_2 (ref. 5). On the other hand, most current atmospheric models do not include aerosol processes because aerosols are not properly monitored on a global scale[6]; their spatial distributions are therefore not known as required for their incorporation in operational GCMs[7,8]. We now attempt to assess aerosol forcing by studying the errors of a GCM without aerosol physics within a data-assimilation system.

In principle, the best estimate of the state of the atmosphere at any given time (referred to here as the analysis) is obtained by data-assimilation systems in which the first guess, determined by a short term forecast with a state-of-the-art GCM, is optimally combined with all available observations[9]. The field differences between the analysis and the first guess are called the analysis increments (or updates) and result, in part, from a complex combination of all model errors due to inadequate representation of physical processes, that is, the model parameterizations, as well as from numerical errors and processes that have been ignored. These increments can be termed as 'model errors'. We note that in the implementation of the GEOS-1 assimilation scheme, the analysis increments are not inserted fully at each analysis time but instead they are gradually inserted over the six-hour period straddling the analysis time. This process is called incremental analysis update, or IAU. The IAU scheme avoids shocking the system, which can lead to spurious oscillations in the assimilating GCM[10].

The study employs 5 years (1985–89) of the NASA GEOS-1 (ref. 11) analysis increments together with dusty days distributions over the Atlantic Ocean, as derived by Jankoviak and Tanre[12]. Dust is the most common aerosol type in the atmosphere. Persistent dust transport over the Atlantic Ocean has been measured in Barbados and Florida[13]. Dust dominates the NOAA images of aerosol over the ocean[8]. About half of the dust is estimated to be associated with anthropogenic sources[3].

Figure 1 (right) shows the monthly averaged number of dusty days for 1984–88 for March, June, September and December, respectively, as derived by Jankoviak and Tanre[12] using an aerosol optical retrieval method based on Meteosat data. It shows an annual cycle in which dust storms from the west Sahara propagate over the Atlantic region at about 11° N in March, gradually shifting to the north to 18° N in June (maximum northward location is at 21° N in August–September, Fig. 2). Also, there is a strong variation in intensity, as expressed by the number of dusty days.

For comparison, Fig. 1 (left) shows the corresponding incremental analysis updates for temperatures, IAU(T), integrated over the dust layer of 650–850 hPa. The 5-yr average is shifted here by 1 year to 1985–89 owing to data availability. The 650–850 hPa layer
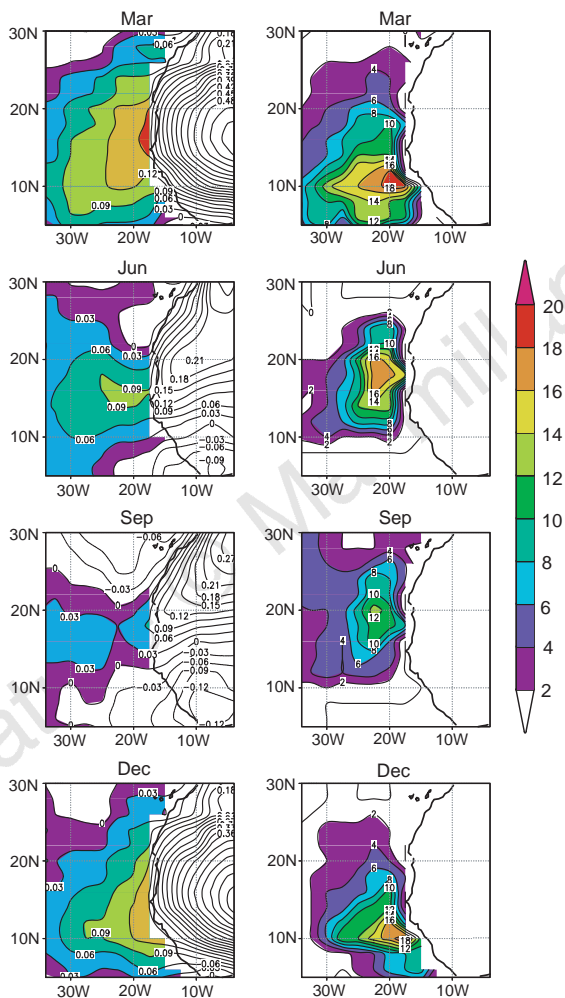
Figure 1 Right, monthly average image of the number of dusty days for five years from 1984 to 1988 for March, June, September and December, top to bottom; taken from ref. 12. Colour represents the number of days in steps of 2, as indicated on the bar to the right. Left, corresponding incremental analysis updates for temperatures, IAU(T), averaged during 1985–89, at the layer of 650–850 hPa. Shading corresponds to positive values over the ocean, which correspond to a warmer atmosphere than predicted by first guess from the model. Contour interval is 0.03 K d^{-1}. Shading calibration is shown on the colour bar on the left. The TIROS (Television Infra-Red Observational Satellite) Operational Vertical Sounder (TOVS) was the primary observational source for the IAU over the ocean[25]. The low-tropospheric TOVS temperature estimates have a slight negative bias over the study domain[25], which suggests that the IAU heating values may be underestimated. The maxima IAU(T) over the ocean of ~0.1 K d^{-1} are close to the maxima found over the whole tropical or subtropical oceans.
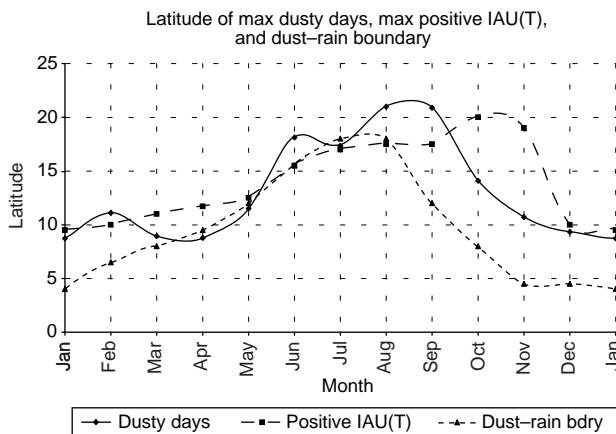
Figure 2 The latitudinal variation of both the maximum IAU(T) (dashed line) and the latitude of maximum dusty days (solid line). The dotted line shows the latitudinal transition of the boundary between the shallow monsoon zone and the zone with convective rainfall (zones B and C1 in ref. 16).

corresponds to about 1.5–3.5 km altitude, typical for Saharan dust layers over the Atlantic[14]. In Fig. 1 (left), shading indicates positive values over the ocean, which correspond to a warmer atmosphere compared with the model first-guess prediction.
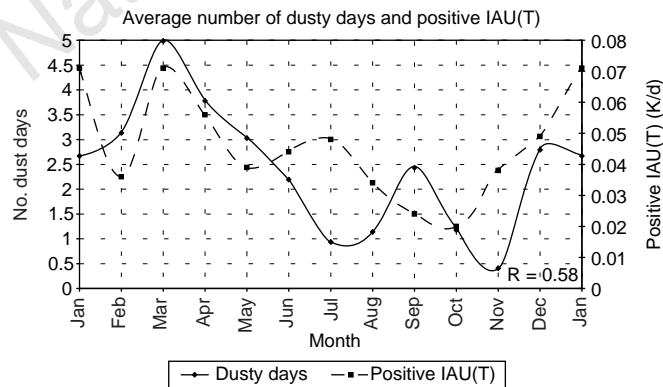
The monthly variation of both the latitude of maximum positive IAU(T) over ocean and the latitude of maximum number of dusty days is shown in Fig. 2. Latitudes of maxima were defined for both curves according to the zonal means over the body of water in the domain 34–4° W. The correlation between the two curves is 0.67 and increases to 0.85 if the latitude of maximum heating is shifted by one month. It suggests that the maximum atmospheric heating in the dust layer lags the maximum in the number of dusty days. The delay may be due to a different process that adds to the IAU(T) seasonal cycle, such as thermal heating of clouds. Indeed, monthly correlation of ISCCP (International Satellite Cloud Climatology Project)[15] low cloudiness and the IAU (not shown) is high during the July–November period, which is the same time as when the dust is weaker (Fig. 3).

There is a strong relationship between the latitudinal transition of the African monsoon boundary and that of the dust (Fig. 2). The dotted line shows the latitudinal transition of the boundary between the shallow monsoon zone and the zone with convective rainfall (zones B and C1 in ref. 16). A similarly high correlation was also found with the latitudinal transition of the Harmattan monsoon sharp wind change from the easterly to westerly sector, but this line (not shown), as expected, precedes both the dust and the IAU; the monsoon rain follows the maximum dust line from the south (Fig. 2) because the rain washes out most of the dust.

There is also a high correlation, r, between the heating rate (K per day) and the number of dust days, $r = 0.58$, as shown in Fig. 3. This relation is given by

$$\text{IAU}(T) = 0.027 + 7.1 \times 10^{-3} \times N_{\text{dust}} \qquad (1)$$

where N_{dust} is the average number of dusty days per box, calculated as the total number of dusty days over the domain divided by the number of grid points. Hence, there is an unexplained heating, that is, heating not due to dust, of 0.027 K per day plus a heating due to dust of up to 0.035 K per day for March. The latter value fits well with the independent most recent model estimations for the longitudinal average latitude belt of 10–30° N (ref. 3). The slope constant in the above equation means that an averaged dusty day causes a monthly averaged heating rate of 7.1×10^{-3} K per day, or
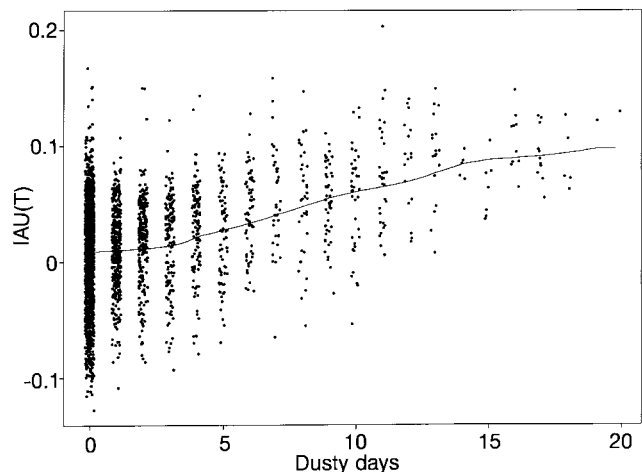
0.21 K per month ($30 \, \text{d} \, \text{m}^{-1} \times 0.0071 \, \text{K} \, \text{d}^{-1}$). However, if we assume that the heating happens only during the dusty-day event, and not during the other days, then this monthly heating rate is really an average of h, the heating rate during the single dusty day, and 29 zero-value heating rates during the other days. Therefore, h, the heating rate during an averaged dusty day, is 0.21 K per day. Maximum heating values over land of 0.5 K per day within the source of dust over the west Sahara also fit very well the model simulations for Saharan dust maximum heating values[17]. The averaged total number of dusty days in a year is 28.6 d yr^{-1}, corresponding to an average heating of 6.0 K yr^{-1} for the full year (28.6 d yr^{-1} × 0.21 K d^{-1}).

The atmospheric response to the dust forcing was also calculated in an alternative and more powerful approach by comparing each dust pixel to the corresponding IAU pixel. Figure 4 is the resulting jittered scatter plot for 2,496 points: 208 points for each month. In contrast to Fig. 3, this comparison contains both the dust/IAU patterns' resemblance for each month and the intermonthly variation. The linear correlation coefficient is 0.41, increasing to 0.48 when the no-dust pixels are omitted. It is interesting to note that the dust forcing deduced from the slope of the curve based on the moving locally weighted regression is 0.19 K d^{-1} (slope for the 3–14 d period multiplied by 30 d), which is quite close to the aforementioned value of 0.21 K d^{-1} derived from the monthly averages. Also, the unexplained bias is reduced from 0.027 K d^{-1} to 0.0062 K d^{-1}, as calculated for a linear regression. The moving locally weighted regression, the kernel regression[18], shows near saturation for a large number of dusty days, that is, when it exceeds 14–15 d. Such a saturation may be expected because the increased number of dusty days also probably reflects an increase in the average dust concentrations.

A similar scatter plot for the relation between IAU and low-level cloudiness from the ISCCP data sets[16] does not reveal any significant correlation, the value being only 0.11. This, however, does not reflect the high positive cloud/IAU correlations we have found for the intermonthly variations because of the high anticorrelated cloud/IAU patterns for December–June (not shown). These complex IAU/cloud relationships are strongly dependent on the cloud parameterizations and conclusive results are therefore impossible to obtain. This is in contrast to the IAU/dust relationship as no dust parameterization was incorporated in the assimilation system.

An independent assessment of the relationship between the

Figure 3 The monthly heating rate in degrees Kelvin per day, as deduced from IAU(T) and the average number of dusty days. The regression relation is given by equation (1), where N_{dust} is the number of dusty days with correlation between the two curves of $r = 0.58$. The unexplained heating of 0.027 K d^{-1} may be due to other deficiencies such as the model's inability to simulate fully the warmth of the Saharan Air Layer. Most of the SAL heating effect on the IAU, however, is below the dust layer.

Figure 4 Jittered scatter plot for IAU(T) versus number of dusty days for each pixel; 208 points for each month total of 2,496 points. A moving locally weighted regression line is plotted and shows the saturation at high number of dusty days. 'Jittered' describes a random spreading of the many points sharing the same value in the close vicinity of the real value, so that the visual information in the graph correctly reflects the number of data points.

aforementioned heating rate and dust radiative forcing can be gained from comparison of the rate of absorption of solar radiation by the dust layer. For example, our measurements from Cape Verde $(16.7°\,N, 23°\,W)$ for 1994–95 suggest an average optical thickness of 0.35 for the dust layer. The heating rate in the 650–850 hPa layer for $\tau = 0.35$ can be estimated from ref. 19 (see their Figs 12, 13) by interpolating values given for $\tau = 0.2$ and $\tau = 0.5$. This procedure gives heating rates of 0.1–$0.2\,K\,d^{-1}$ for the cloud-free ocean case, and up to 0.3–$0.5\,K\,d^{-1}$ in the cloud case, which fits well with our estimations for an average dust event of $0.21\,K\,d^{-1}$ or $0.19\,K\,d^{-1}$ (derived from Figs 3 and 4, respectively).

Another comparison can be made with most recent modelling results from Tegen et al.[3], who indicate that the average mean global optical thickness coming from disturbed soil is 0.017. To retrieve our mean value (0.35), we have to assume that dust with $\tau = 0.35$ is covering 5% of the total Earth's surface. As dust is located between $10°$ and $30°\,N$, approximately one-third of the 10–$30°$ latitude belt would be covered by a dust cloud of $\tau = 0.35$. They further indicate that the longitudinal mean heating between $10°$ and $30°\,N$ is $0.04\,K\,d^{-1}$: this would result in a heating rate that is three times larger where dust is located, or $0.12\,K\,d^{-1}$.

There is also a dynamical heating effect on the IAU due to the Saharan air layer (SAL). This, however, has a different spatial and temporal signature from dust and concentrates in a lower-altitude layer[20]. The sporadic heating due to the dust at a particular time and location is determined by the transient local properties of a travelling dust plume—the local dust profile and dust content—whereas that of the SAL is on a larger (synoptic) scale. Therefore, dust plume heating is superposed locally and perhaps semirandomly on that of the SAL. The model is sensitive to the general presence and intensity of the SAL but does not contain dust. The product of the data assimilation system—the IAU—does include the effects of dust and thus can show the much more rapidly variations in local conditions due to the passing of a dust plume. Also, the vertical profiles of both the IAU and the theoretical diabatic heating due to Saharan dust[19] show a sharp increase in the 750–580 hPa layer which is located with the average upper part of the dust layer; the climatological SAL profiles, however, indicate a peak in the heating rate below 900 hPa.

We have also compared the global seasonal $IAU(T)$ for 1987 with equivalent atmospheric optical thicknesses (EAOT) maps from Husar et al.[8]: this indicates that the pattern similarities between $IAU(T)$ and EAOT exist not only over the Atlantic Ocean but also over other dusty regions, including the Indian Ocean, the Bay of Bengal and the south China sea during spring and summer (not shown).

This work indirectly shows the response of the temperature field to the radiative forcing of the dust layer. The resulting heating rate of $6\,K\,yr^{-1}$ within the dust layer at 1.5–3.5 km is in agreement with calculated heating rates[17,20–22] and therefore may be used for improving atmospheric predictions once dust loading is monitored daily by satellite, as is planned for the MODIS (Moderate Resolution Imaging Spectroradiometer) instrument on the Earth-observing system[23,24]. □

1. Charlson, R. et al. Climate forcing by anthropogenic aerosols. Science 255, 423–430 (1992).
2. Penner, J. E. et al. Quantifying and minimizing uncertainty of climate forcing by anthropogenic aerosols. Bull. Am. Meteorol. Soc. 75, 375–400 (1994).
3. Tegen, I., Lacis, A. A. & Fung, I. The influence of mineral aerosols from disturbed soils on the global radiation budget. Nature 380, 419–422 (1996).
4. Arking, A. The radiative effects of clouds and their impact on climate. Bull. Am. Meteorol. Soc. 72, 795–813 (1991).
5. Lindzen, R. S. Some coolness concerning global warming. Bull. Am. Meteorol. Soc. 71, 288–299 (1990).
6. Moulin, C., Lambert, C. E., Dulac, F. & Dayan, U. Control of atmospheric export of dust from North Africa by the North Atlantic Oscillation. Nature 387, 691–694 (1997).
7. Prospero, J. M. et al. Temporal variability of summertime ozone and aerosols in the free troposphere over the eastern North Atlantic. Geophys. Res. Lett. 22, 2925–2928 (1995).
8. Husar, R. B., Prospero, J. M. & Stowe, L. L. Characterization of tropospheric aerosols over the oceans with the NOAA advanced very high resolution radiometer optical thickness operational product. J. Geophys. Res. 102, 16889–16910 (1997).
9. Daley, R. Atmospheric Data Analysis (Cambridge Univ. Press, New York, 1991).
10. Bloom, S. S., Takacs, L. L., da Silva, A. M. & Ledvina, D. Data assimilation using incremental analysis updates. Mon. Weath. Rev. 124, 1256–1271 (1996).
11. Schubert, S. et al. An assimilated data set for Earth Science applications. Bull. Am. Meteor. Soc. 74, 2331–2342 (1993).
12. Jankoviak, I. & Tanre, D. Satellite climatology of Saharan dust outbreaks: Method and preliminary results. J. Clim. 15, 646–656 (1992).
13. Prospero, J. M. & Nees, R. T. Impact of the North African drought and El Niño on the mineral dust in the Barbados trade winds. Nature 320, 735–738 (1986).
14. Westphal, D. L., Toon, O. B. & Carlson, T. N. A two-dimensional numerical investigation of the dynamics and micro-physics of Saharan dust storms. J. Geophys. Res. 92, 3027–3049 (1987).
15. Rossow, R. B. & Schiffer, R. A. ISCCP cloud data products. Bull. Am. Meteorol. Soc. 72, 2–20 (1991).
16. Asnani, G. C. Tropical Meteorology (Indian Inst. of Tropical Meteorology, Pune, 1993).
17. Pick, C. Transport of Desert Aerosols and their Influence on Local Temperature and Motion. Thesis, Tel Aviv Univ. (1991).
18. Eubank, R. L. Spine Smoothing and Non-parametric Regression (Dekker, New York, 1988).
19. Carlson, T. N. & Benjamin, S. G. Radiative heating rates for Saharan dust. J. Atmos. Sci. 37, 193–213 (1980).
20. Karyampudi, V. M. A Numerical Study of the Evolution, Structure and Energetics of the Saharan Air Layer. Thesis (Pennsylvania State Univ., 1986).
21. Joseph, J. H. in Aerosols and their Climatic Effects (eds Gerber, H. E. & Deepak, A.) 215–226 (Deepak, Hampton, VA, 1984).
22. Alpert, P. & Ganor, E. A jet-stream associated heavy dust storm in the western Mediterranean J. Geophys. Res. 98, 7339–7349 (1993).
23. Tanré, D., Kaufman, Y. J., Herman, M. & Matoo, S. Remote sensing of aerosol over oceans using the EOS-MODIS spectral radiances. J. Geophys. Res. 102, 16971–16988 (1997).
24. Kaufman, Y. J. et al. Remote sensing of tropospheric aerosol over land from EOS moderate resolution imaging spectroradiometer. J. Geophys. Res. 102, 17051–17068 (1997).
25. Reale, A. L., Chalfant, M. W., Wagoner, R. V., Gardner, T. J. & Casey, L. W. TOVS Operational Sounding Upgrades 1990–1992. NOAA Tech. Rep. NESDIS 76 (US Dept of Commerce, NOAA NESDIS, Washington DC, 1994).

Evidence for long-term diffuse deformation of the lithosphere of the equatorial Indian Ocean

Richard G. Gordon[*], **Charles DeMets**[†] & **Jean-Yves Royer**[‡]

[*] Department of Geology & Geophysics, Rice University, Houston, Texas 77005, USA

[†] Department of Geology & Geophysics, University of Wisconsin, Madison, Wisconsin 53706, USA

[‡] Géosciences Azur, CNRS UMR 6526, BP48, 06235 Villefranche-sur-Mer cedex, France

The presence of large earthquakes, east–west-striking folds and thrust faults in sediments, and east–west-striking undulations of wavelength 200 km in topography and gravity shows that the equatorial Indian Ocean is the locus of unusual deformation[1–8]. This deformation has been interpreted as a diffuse boundary between two tectonic plates[9–13]. Seismic stratigraphy and deep-sea drilling at two locations in the Bengal fan indicate that the deformation began 7.5–8.0 Myr ago[3,14,15]. Here, however, we show, using plate reconstructions, that motion across this diffuse oceanic plate boundary began more than 10 Myr earlier than previously inferred and that the amount of north–south convergence across the boundary through the central Indian basin has been significantly greater than the convergence estimated from seismic profiles. The relative plate velocity accommodated across the central Indian basin has varied with time and has been as fast as $\sim 6\,mm\,yr^{-1}$—about half the separation rate of Earth's slowest-spreading mid-ocean ridge. The earliest interval of measurable motion, which began more than 18 Myr ago, may coincide with rapid denudation of the Tibetan plateau from ~ 21 Myr to 15–17 Myr (ref. 16). The present motion across the central Indian basin began no earlier than 11 Myr—following an earlier interval of slower motion from 18 to 11 Myr—and may have begun at ~ 8 Myr, when the Tibetan plateau is thought to have attained its maximum elevation[16,17].